Evolution and Features of Dust Devil-Like Vortices in Turbulent Rayleigh-Bénard Convection – An Experimental Study

Christian Kaestner[1], Julien David Schneider[1], and Ronald du Puits[1]

[1]Institute of Thermodynamics and Fluid Mechanics, Technische Universitaet Ilmenau, Ehrenbergstr. 29, 98693 Ilmenau, Germany

Key Points:

- dust devils
- particle tracking velocimetry
- Rayleigh-Bénard convection
- turbulence

Corresponding author: Christian Kaestner, christian.kaestner@tu-ilmenau.de

Abstract

We present an experimental study simulating atmospheric dust devils in a controlled laboratory experiment. Our work complements and extends the numerical work of Giersch and Raasch (2021) by experiments. Dust devils are thermal convective vortices with a vertical axis of rotation visualized by entrained soil particles. They evolve in the convective atmospheric boundary layer and are believed to substantially contribute to the aerosol transport into the atmosphere. Thus, genesis, size, lifetime and frequency of occurrence of dust devils are of particular research interest. Extensive experimental studies have been conducted by field measurements and laboratory experiments. Field measurements lack of unpredictable formation of dust devils and limited area to be observed. Hitherto laboratory experiments, which frequently generate dust devils with fans, lack of generic conditions in the atmosphere. In our study, we investigate dust devil-like vortices in a large-scale Rayleigh-Bénard experiment. This set-up mimics the natural process of dust devil formation as closest to reality so far. The flow measurement was carried out by particle tracking velocimetry using neutrally buoyant soap bubbles. We identified initial dust devil-like vortices by eyes from the Langrangian velocity field and in a later more sophisticated analysis by a specific algorithm from the Eulerian velocity field. We analyzed their frequency of occurrence, observation time and size. With our work, we could demonstrate that turbulent Rayleigh-Bénard convection is an appropriate model to mimic the natural process of the genesis of dust devil-like vortices in the thermal boundary layer of the atmosphere without any artificial stimulation.

1 Introduction

Dust devils are medium-scale convective vortex structures with vertical rotational axis appearing at ground level of the atmosphere. They are detected in terrestrial and Martian atmosphere (Balme & Greeley, 2006). Dust devils occur, when hot air near a solar heated surface hot spot rises quickly through the cooler air layer above. The thermal convective phenomenon is initiated by "superadiabatic lapse rate" (Balme & Greeley, 2006) at the insulated surface and continues as plume outside the thermal boundary layer (Sinclair, 1969). Under certain conditions, e.g. local vortices initiated by convection or distracted wind at obstacles, the up-drafting air starts to rotate (Balme & Greeley, 2006; Carroll & Ryan, 1970; Renno et al., n.d.). Due to vertically stretching of the uprising column of hot air, entrained dust moves towards the axis of rotation. Thus, conservation of angular momentum leads to increased tangential velocity at smaller radii, and hence, an enhancement of the spinning effect. A secondary flow induced by the pressure drop sucks further hot air horizontally from the surface inward to the bottom of the initial vortex structure (Metzger, 1999). Thus, the spinning effect continuously intensifies as more hot air rushes and raises and the vortex becomes self-sustaining and forms a fully developed dust devil (Sinclair, 1969, 1973). Thus, a fully developed dust devil appears as a funnel-like chimney (columnar, V-shaped or just disordered, rotating dust cloud) in which inside air circulates and moves upwards (Metzger, 1999). During the uprising process, the hot air cools down and buoyancy gradually cancels until air stops to rise. The rising hot air inside the vortex core displaces cool air descending at the outside of the vortex core. This balancing effect against the spinning hot-air outer wall stabilizes the dust devil (Ludlum, D. M. W. and Society, N. A., 1991). Surface friction besides the rotary motion generates a forward momentum causing the dust devil to move around on the surface, and frequently being tilted up to 10 degree in forward direction (McGinnigle, 1966; Sinclair, 1973). Further impulsion, sustaining or even feeding the dust devil, may be gained by passing further surface hot spots. The size of dust devils ranges from a few meters up to over 1 km in height. They are usually at least 5 times higher than wide, with wind speeds of up to 25 m/s (Bell, 1967; Flower, 1936; Hess & Spillane, 1990; Sinclair, 1965; Williams, 1948). Their lifetime ranges from only a few minutes up to several hours, whereby lifetime correlates with height as 1 hour for each 300 m of height (Idso & Kimball, 1974; Ives, 1947; Mattsson et al., 1993; Metzger, 1999). Beneficial for the formation of dust devils are arid, hot, flat surfaces with gentle slope and regions with strong horizontal

thermal gradients (Brooks, 1960; Mattsson et al., 1993; Sinclair, 1969). The frequency of occurrence is inversely related to their size (Carroll & Ryan, 1970). Moreover, there is no preferred direction of rotation which indicates that their size is too small to be affected by Coriolis force (Morton, 1966).

A lot of experimental effort has been spent to investigate dust devils in their natural environment. Originally, dust devils were visually observed, obtaining statistics of features, motion and frequency. Additionally, sensors like anemometers, pressure gauges and temperature probes allowed to investigate the inner structure and composition of a dust devil. Within the pioneering work of Sinclair (1969), sensor arrays were pushed into the vortex to characterize the inner structure of a dust devil. Other authors report that they applied drones to fly the instrumentation inside the dust devil (Jackson et al., 2018), placed stationary sensors at the ground (Lorenz et al., 2015), or used LIDAR (light detection and ranging) (Chan & Li, 2021) to investigate dust devils. Anyhow, all these methods, except drones, only provide usable data when a dust devil passes the sensors by chance. Non-invasive, contactless measurements, e.g. optical or spectroscopic methods, are not applicable or extremely affordable to apply. However, this is the only option to not change the vortex structure by the measurement process itself due to physical interaction between sensor and flow. In general, field studies are often time consuming and require comprehensive technical equipment, almost interfere with the flow structure of the dust devils and do not allow continuous in-situ sensing during their whole lifetime.

Thus, there is certain interest to perform laboratory experiments. Several studies were conducted to mimic the genesis of dust devils in laboratory experiments. First attempts were rotating hot plates, applying constant rotational momentum to a convective updraft (Barcilon, 1967; Fitzjarrald, 1973). These studies lacked accurate boundary conditions and the flow was often just laminar. Another way was to apply fans to generate a rotating channelized flow which was supposed to apply more realistic boundary conditions (Maxworthy, 1972; Mullen & Maxworthy, 1977). A great advancement and a more sophisticated way of mechanical genesis of dust devil-like vortices was the Arizona State University vortex generator (ASUVG) (Balme et al., 2001; Greeley et al., 2003; Neakrase & Greeley, 2010). Nevertheless, even this laboratory device is not fully capable to model the original process of dust devil genesis exclusively driven by natural thermal convection. Ringrose (2005) presented an approach very close to the natural environment. They used a heated metal plate surrounded by a wall of Perspex windows, comparable to Bénard-Marangoni convection. But, due to the chimney-like structure of this convection cell, the formation of dust devils is artificially amplified and remains still far from the original boundary conditions in the atmosphere.

Complementary numerical studies are almost based on large-eddy simulations (LES) which reduce computational time at larger domains compared to direct numerical simulations (DNS) (Giersch et al., 2019; Kanak, 2005). Since dust devils are only medium-scale structures compared to the entire atmospheric boundary layer, the spatial resolution of LES is often not sufficiently well (only a few meters) to resolve the inner structure of a dust devil. In particular, the surface layer as source of dust devils is inadequately resolved by sub-grid scale (SGS) models (Ohno & Takemi, 2010; Raasch & Franke, 2011; Sorbjan, 1996; Spiga et al., 2016; Sullivan et al., 1994). A further deficit of LES exhibits considering the potential kind of the formation of dust devils. They are believed to appear at the updraft inclination point of two large-scale atmospheric convection roles. Whilst LES is able to resolve such large convection rolls nicely, the local fluctuations and small vortices which initiate the rotation of up-drafting hot air in the surface layer cannot be resolved. In order to overcome this problem, direct numerical simulations (DNS) which are able to resolve the flow field down to the smallest vorticies would help. There is some related work on Rayleigh-Bénard convection (RBC), but with increasing size of the computational domain and the period to be simulated, the computational effort quickly increases beyond the actual capabilities (Cortese & Balachandar, 1993; Fiedler & Kanak, 2001; Giersch & Raasch, 2021).

In our study, we present a new experimental approach to generate dust devils under natural boundary conditions. We use turbulent RBC at a width-to-height ratio of 3 to mimic the conditions of the convective atmospheric boundary layer and to study potentially occurring vortex phenomena of the lower atmosphere (Fodor et al., 2019). Giersch and Raasch (2021) conducted DNS under same boundary conditions as applied in this experimental study and could finally detect dust devil-like vortices in their simulations. Our experiments will complement these numerical simulations, even though, we will not be able to detect and to measure the vortices down to the centimeter scale. The benefit of our experiment is that it ran for about 22 h covering a much longer period than the 100 s in the DNS. The extended measuring time improves the statistics, especially the probability of catching larger dust devil-like vortices. This improvement finally complements the numerical results by expanding the range of detected structure size, but also contributes to validate the DNS model.

2 Methodology

2.1 Concept

To simulate the genesis of dust devil-like vortices close to their natural origin in the convective boundary layer of the Earth's atmosphere, experiments were conducted in a large-scale Rayleigh-Bénard cell called "Barrel of Ilmenau". This is an idealized experimental set-up to study natural thermal convection. RBC is a canonical well-known set-up, which consists of a fluid layer uniformly heated from below, uniformly cooled from above and obeys adiabatic sidewalls. Similar to the convective atmospheric boundary layer, temperature is decreasing from bottom surface with increasing height. The experiment is equivalently adjusted to a larger horizontal elongation compared to the vertical extent. Furthermore, due to the fact that condensation and radiation effects do not account for the genesis of dust devils, RBC is a perfect experimental model to study dust devils. The Rayleigh-Bénard set-up is characterized by totally five dimensionless numbers (Lienhard & John, 2005). The degree of turbulence may be described by the Rayleigh number Ra and can be regarded as the relation between buoyancy and viscous forces:

$$Ra = \frac{g\beta(T_h - T_c)L^3}{\nu\kappa}. \tag{1}$$

The Prandtl number Pr depicts the relation between viscosity and thermal diffusivity:

$$Pr = \frac{\nu}{\kappa} = \frac{\eta}{\rho\kappa}. \tag{2}$$

The Reynolds number Re describes the relation between inertia and viscous forces:

$$Re = \frac{uL}{\nu} = \frac{\rho uL}{\eta}. \tag{3}$$

The Nusselt number Nu is the ratio of convective and conductive heat transfer:

$$Nu = \frac{hL}{\lambda}. \tag{4}$$

In these definitions, ρ is the density of the fluid, ν the kinematic viscosity, η the dynamic viscosity, u the velocity, κ the thermal diffusivity, g the acceleration due to gravity, β the thermal expansion coefficient, λ the thermal conductivity, h the convective heat transfer coefficient, L the characteristic linear dimension in vertical direction, T_h the surface temperature of the hot plate and T_c the surface temperature of the cold plate. A further dimensionless number, characterizing the ratio of the horizontal extent W and the vertical extent L of the convection cell is the aspect ratio Γ:

$$\Gamma = \frac{W}{L}. \tag{5}$$

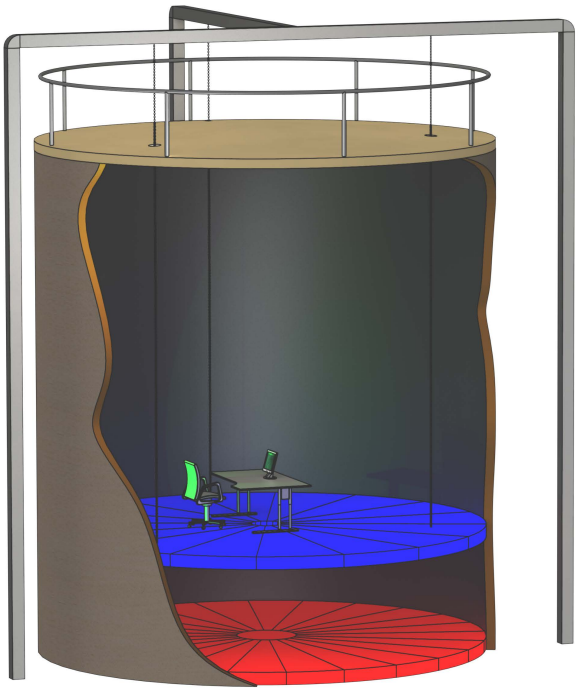

Figure 1: Schematic of the "Barrel of Ilmenau".

Our Rayleigh-Bénard cell has a cylindrical shape with a diameter $W = 7.15$ m and a height $L = 2.38$ m resulting in an aspect ratio of three. A schematic of the "Barrel of Ilmenau" is shown in Figure 1. The large size of the convection experiment allows to set a turbulent flow in this specific geometry with Rayleigh numbers up to $Ra = 5 \times 10^{10}$. It furthermore enables the reproduction of large-scale convective flow structures which can be measured using optical measurement techniques. The bottom and top plates were heated and cooled to distinct temperatures, respectively, applying Rayleigh numbers in the range of $1 \times 10^{10} < Ra < 2 \times 10^{10}$. Even though, this is far from the Rayleigh number of the atmospheric boundary layer with $Ra \approx 10^{18}$, the simulations by Giersch and Raasch (2021) confirmed Rayleigh numbers $Ra \approx 10^{10}$ to be sufficiently high to generate dust devil-like vortices. The Prandtl number was $Pr = 0.71$ for air as working fluid. The wall was equipped with a thermal compensation system to keep adiabatic boundary conditions (Du Puits et al., 2013). We applied four different settings to study the genesis of dust devil-like vortices in turbulent RBC. In a first set-up, we measured the flow almost in the entire fluid volume. This measurement serves to evaluate the global flow pattern and to validate the existence of multiple convection rolls at the chosen geometry. The latter one is believed to be a necessary condition that dust devils emerge. The disadvantage of this set-up is that we can discover only vortices with diameters of about 50 cm or larger. This is far beyond those ones, Giersch and Raasch (2021) reported from their DNS. As a consequence, we reduced the field of view of the optical measurement (see below for a detailed description) to a volume of about 4 m^3 which increased the resolution of the measurement and enabled us to detect even smaller vortices down to about one decimeter. In order to increase the probability of the occurrence of dust devil-like vortices, we placed an additional heating foil of 480 mm by 580 mm at the center of the heating plate. Similar as in nature, this generates a local hot spot with a typical over temperature of about $\Delta T = 17$ K with respect to the temperature of the heating plate and may help to produce a larger number of vortices compared to the uniformly heated bottom plate.

2.2 Instrumentation

2.2.1 Particle Tracking Velocimetry

Particle tracking velocimetry (PTV) is an optical flow measurement technique. The fluid flow is seeded with particles which are illuminated by a light source. The light backscattered from the particles is detected using a single (planar PTV) or multiple (3-d PTV) cameras. The vectors of velocity and acceleration of the particles are identified from their displacement and the time interval between two frames. Since each particle is tracked individually with time, the Lagrangian velocity field of the flow is obtained. The spatial resolution depends on the density of particles in the measurement volume. On the other side, the number of particles cannot be arbitrarily increased, because they must be identified one-to-one in successive recordings. For a volumetric flow measurement, multiple cameras are used to reconstruct the 3-d particle position for each recording. A synchronization between the cameras as well as with the light source is required.

2.2.2 Tracers

Particle based flow measurement essentially requires tracer particles that virtually follow the motion of the surrounding fluid slip-free. Moreover, the particles should feature the same density as the surrounding fluid, because otherwise, they will exhibit an artificial velocity component with or against the vector of gravity. For our experiments, they also have to be sufficiently large to be captured by the cameras at each position in the flow field. Typically used Di-Ethyl-Hexyl-Sebacat (DEHS) for particle image velocimetry are not appropriate, since the particle diameter is of the order of only 1 μm. However, our optical set-up requires particles with a diameter of at least a few millimeters to get detected even at a distance of about 7 m from the cameras. Here, helium filled soap bubbles turned out as ideal candidates. The helium applies the necessary buoyancy to the heavier soap bubble envelope and equilibrates the bubble density to the density of the surrounding air. Bubble size and envelope thickness D are linearly correlated if density of tracers and fluid are considered equal. Since the surface area S of the bubble grows with the square of the radius R, the evaporation rate of the soap liquid grows in the same manner. This decreases the lifetime/stability of the soap bubbles when their radius increases. If considering linear correlation between surface area and evaporation rate, envelope thickness decreases transiently faster due to evaporation compared to the initial growth due to bubble size. Thus, tracers should be as small as possible for elongated lifetime, but as large to be detectable by the cameras. We have identified bubble diameters of about 5 mm and 3 mm as an appropriate size for the two different set-ups.

A dimensionless number that describes the ability of a particle to follow the motion of a surrounding fluid is the Stokes number St. It is defined as the ratio of relaxation time t_r of the particle and the characteristic time scale of the flow. For the following analysis, we use the free-fall time t_f which is a characteristic time scale for fast dynamics of thermal plumes and vortices in turbulent RBC (Pandey et al., 2018). These quantities are defined as follows:

$$St = \frac{t_r}{t_f} \qquad t_r = \frac{\rho_p d_p^2}{18\nu} \qquad t_f = \sqrt{\frac{L}{g\beta\Delta T}} \tag{6}$$

with ρ_p and d_p being the particle density and diameter. Three domains for the Stokes number can be determined:

- $St \ll 1$: particles follow the continuous phase of the flow
- $St \approx 1$: strong interaction between particle and continuous phase
- $St \gg 1$: particles detach the continuous phase of the flow

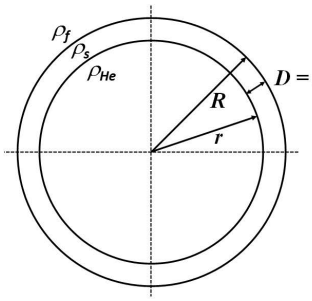

$$D(R) = \left(1 - \sqrt[3]{\frac{\rho_f - \rho_s}{\rho_{He} - \rho_s}}\right) \cdot R \quad , \quad S(R) = 4\pi R^2$$

$\boldsymbol{\rho_f}$: fluid density, $\boldsymbol{\rho_s}$: soap density, $\boldsymbol{\rho_{He}}$: helium density,
$\boldsymbol{D}$: envelope thickness, $\boldsymbol{R}$: bubble radius, $\boldsymbol{S}$: surface area

Figure 2: Soap bubble – definition of envelope thickness and surface area.

In our experiments the Stokes number of the helium filled soap bubbles amounts to about 0.01 to 0.04 which means the bubbles almost perfectly follow the large-scale pattern of fluid flow. Besides their ability to follow the flow, the soap bubbles should be neutrally buoyant. This happens due to a natural selection process. Bubbles lighter than the surrounding air will quickly move upwards, hit the cold plate and burst. Heavier bubbles will fall down, hit the hot plate and burst. Eventually only the neutrally buoyant bubbles will remain in the fluid flow. The particle diameter was about 5 mm for the measurements covering the entire volume of the convection cell. In case of the higher resolved measurements with a reduced field of view, the diameter was reduced to about 3 mm, which led to longer lived tracers and higher particle density. The achieved particle density, resulting in active tracks in our experiments, was up to 22 m^{-3}. Assuming a roughly homogeneous distribution of the tracks in space, this is a sufficient number to investigate the global flow or local coherent flow structures of larger decimeter scale. In the higher resolved experiments, the density was up to 100 m^{-3}, which allowed the detection of smaller structures on a lower decimeter scale. This is of the order of the largest, but still also of the rarest dust devil-like vortices obtained in the numerical simulations by Giersch and Raasch (2021). However, due to the much longer observation time in our experiments, we could detect and characterize as well a reasonable number of such vortices.

2.2.3 Camera set-ups, calibration and measurement procedure

For all measurements, we used four cameras GO-5000M-USB (JAI Technology Co., Ltd.) with a resolution of 2560 by 2048 pixels to record the particle motion. The cameras were either equipped with 8.5 mm lenses LM8XC (KOWA optronics Co., Ltd.) to capture the entire volume of the convection cell or with 25 mm lenses LM25XC for the reduced field of view. Illumination of the particles was applied with five high power LEDs (Luxeon), fixed at the wall. One LED was placed at the center between the cameras and the rest at the sidewall of the experiment, perpendicular to the optical axis of the camera system, left and right, each two. The field of illumination and fields of view are depicted in Figure 3. The cameras and LEDs were synchronized and work with a repetition rate of 10 Hz in set-up I and 20 Hz in set-up II. The recording time for a single run was about two hours and limited by the capacity of the data storage system (one hour for the reduced field of view). In order to assign the "world (3D)" coordinates to the coordinates of the four camera images, a calibration is required. This calibration was performed using a custom made 2D calibration plate of 1000 mm x 800 mm for the full-scale measurement set-up. It was subsequently placed at 30 random positions spanning the entire field of view in this set-up. We took multiple images with each of the cameras and used the mean of these images to reassign "world (3D)" to "image (2D)" coordinates. The algorithm used for this procedure is based on the pinhole model and solves a system of nonlinear equations. In order to increase the accuracy of the calibration, we applied a subsequent volume self-calibration

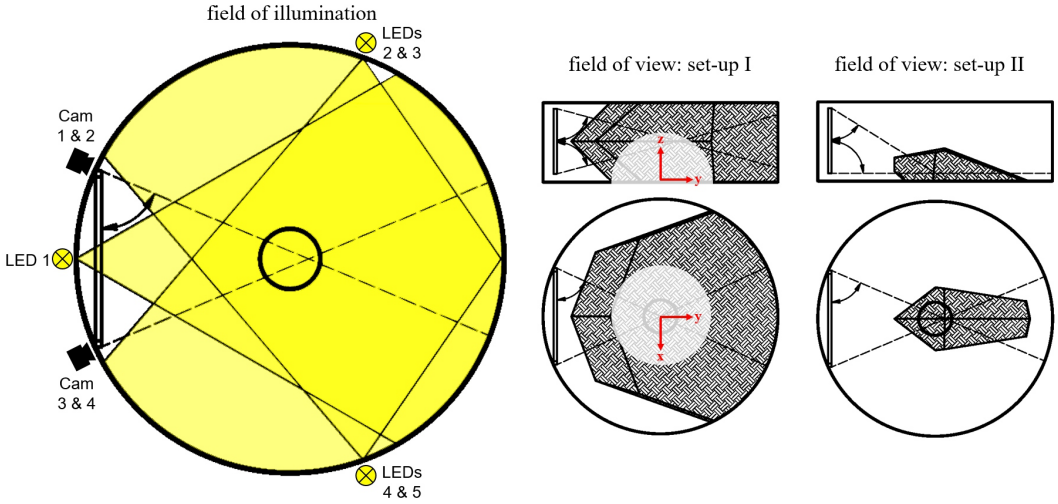

Figure 3: Field of illumination and fields of view for both set-ups measuring large and reduced volume of the convection cell.

algorithm (Wieneke, 2018). This algorithm uses the acquired particle images for the triangulation of real particles in the flow and refines the calibration parameter of the cameras (position, inclination, rotation, focal length of the lenses). For set-up II with the reduced field of view, we used a higher resolving 2D calibration plate which has been imaged in three equidistant parallel positions along the optical axis. The calibration plate covers nearly the entire field of view in this set-up and a polynomial mapping could be used for calibration. It was also followed by the volume self-calibration algorithm. The soap bubbles, we used to make the air flow "visible" in the test section, were injected using two particle generators. They were located in a height of about 1 m above the heating plate. The generators continuously seeded the flow with bubbles diametrically from the wall into the bulk. In order to prevent any significant disturbance of the flow, we took care to keep a sufficiently large distance towards the field of view. The camera images were processed with commercial software package DaVis. Particle tracks were reconstructed using the Shake-the-Box algorithm (Schanz et al., 2016). Further data analysis was proceeded using homemade Matlab code. More details on the experimental set-up and the measurement procedure can be found elsewhere (Loesch & du Puits, 2020, 2021).

2.3 Validation of experiment

Before we started with the search and the analysis of dust devil-like vortices in the RB flow, we have validated the measurement set-up. An appropriate method to do this is comparing the probability density functions (PDF) of the single components of the measured velocity fields. Since we consider a turbulent flow in a closed container and the measured Lagrangian field spans almost the complete volume of the convection cell, the PDFs of the velocity and the acceleration should be symmetrically around zero. We also wish to note here that only the flow field in the turbulent and well-mixed bulk is considered for this analysis. The boundary layers close to the walls are too small and cannot be resolved. A typical deviation from symmetry that may occur is a velocity or acceleration offset induced by the particle injection, i.e. the airflow of the particle generator causes an artificial momentum. This argumentation is true, if the degree of turbulence is large and the applied momentum is low. We analyzed the measured Langrangian fields and check whether the velocity of particles is homogeneously distributed in the volume. On shorter periods transient local events with large coherence may lead to stronger deviation of the PDFs, but will

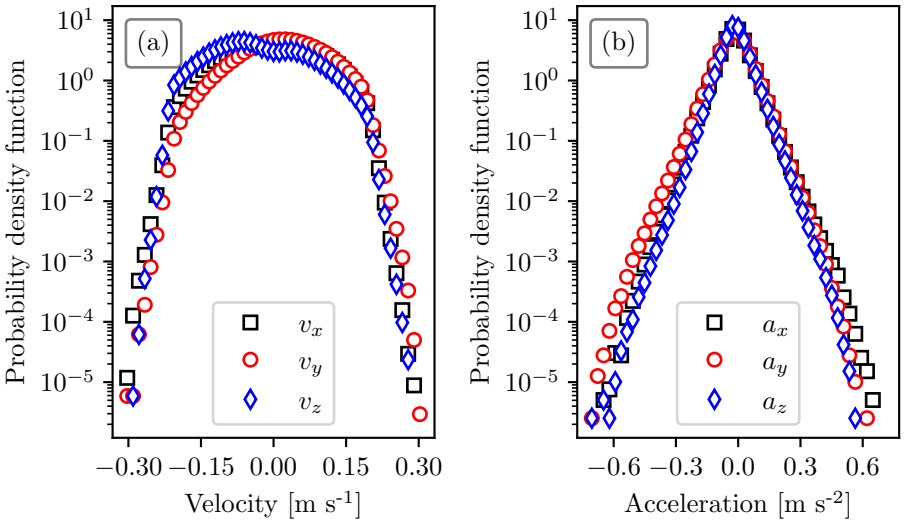

Figure 4: Propability density functions (PDF) of a) velocity and b) acceleration on a long period of about 5200 s.

diminish on longer periods. Figure 4 shows the PDFs of velocity and acceleration components on a long period of about 5200 s in the large volume (set-up I). The most-likely symmetric distribution of all PDFs confirms a homogeneously distributed particle velocity, acceleration and density, respectively.

2.4 Detection and analysis of dust devil-like vortices

Detection of dust devil-like vortices directly from the Lagrangian velocity field is quite hard since particle tracks are spaced very unevenly, and moreover, they are broken very frequently. Thus, we have developed a 2-step detection algorithm which is based on transformation of the Lagrangian velocity field in a grid-based Eulerian velocity field and a subsequent algorithm to identify vortical structures with a vertical axis and a significant pressure drop in their center. In the first step the Eulerian velocity field is reconstructed by binning the particle tracks to a regular grid spacing of $50\times50\times50$ mm^3 using quadratic polynoms. Then, the velocity field is checked in a 7×7 matrix around every grid point in each horizontal plane for the existence of a vortical flow field. Those grid points fulfilling this criterion are selected as potential candidates for a dust devil-like vortex. In the second step the Eulerian velocity field is refined by a so-called fine-scale reconstruction algorithm (Jeon et al., 2018). Here, the Eulerian field is reconstructed by direct numerical simulation of the Navier-Stokes and continuity equations with boundary conditions (velocity and acceleration) taken from the Lagrangian field and under conservation of vorticity. This procedure provides along with the velocity field also the pressure field and enables us to apply also the pressure criterion for the detection of dust devil-like vortices, according to the scheme introduced by Raasch and Franke (2011). Having found the candidates of dust devil-like vortices, we characterize their size, observation period and frequency of occurrence. Unfortunately, we cannot provide the real lifetime of the structures, since they pass only a limited time in the observation area and some of them already exist before they enter the observation area and some others still exist after leaving it. The extracted data is defined by the following convention: time averaged values $\bar{\cdot}$, maximum values $\widehat{\cdot}$ and to the vortex center tangentially averaged values $\{\cdot\}$.

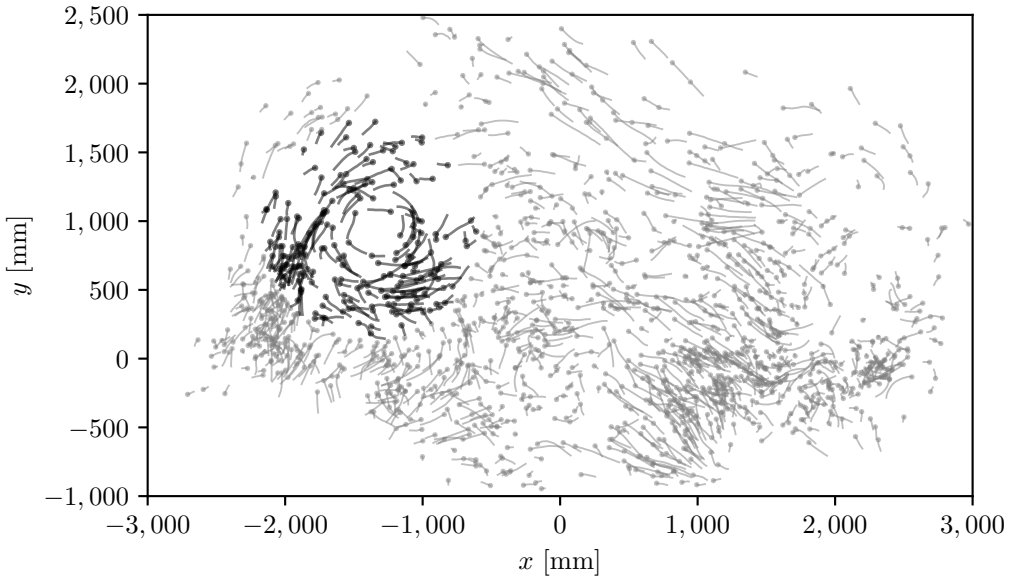

Figure 5: Large scale dust devil-like vortex detected in full-scale measurement at "Barrel of Ilmenau". Projection of the 3D trajectories in a horizontal plane. The dust devil-like vortex (black trajectories) is emphasized.

3 Results and discussion

First, we wish to present a dust devil-like vortex we could observe during the full-scale measurements (see Fig. 3). The vortex was visually detected following the Lagrangian trajectories of the soap bubbles by eye and looking for circular streamlines. However, we could detect only two such structures in 20 hours measurement period, whose diameter were of the order of about 800 mm. Both vortices originated at the heating plate and extended to half height of the convection cell. This happens due to the symmetric structure of the RBC which is one of the distinguishing facts with respect to the convective atmospheric boundary layer. The symmetry of RBC also may trigger dust devil-like vortices to start at the cooling plate and to extend in direction of the gravity vector to maximum half height of the convection cell. Figure 5 shows one of these two dust devil-like vortices whose lifetime amounted to about 18 s. Unlike expected, this vortex did not migrate along a path but it only tumbled around one fixed position. We attribute this particular behavior to the comparatively small volume of our RB cell whose diameter is only seven times the diameter of the vortex.

Unfortunately, it was not possible to detect smaller dust devil-like structures in this set-up, since the particle density and the optical resolution of the cameras were too small. Therefore, we decided to reduce our measurement volume to about 3 m^{-3} (compare set-up II in Fig. 3) which enhanced the optical resolution in the measurement volume. Moreover, we could inject the soap bubbles more targeted which increased the seeding density. This modification enabled us to detect dust devil-like vortices down to one decimeter and pushed up the detection rate from two dust devil-like vortices within 20 hours measurement time

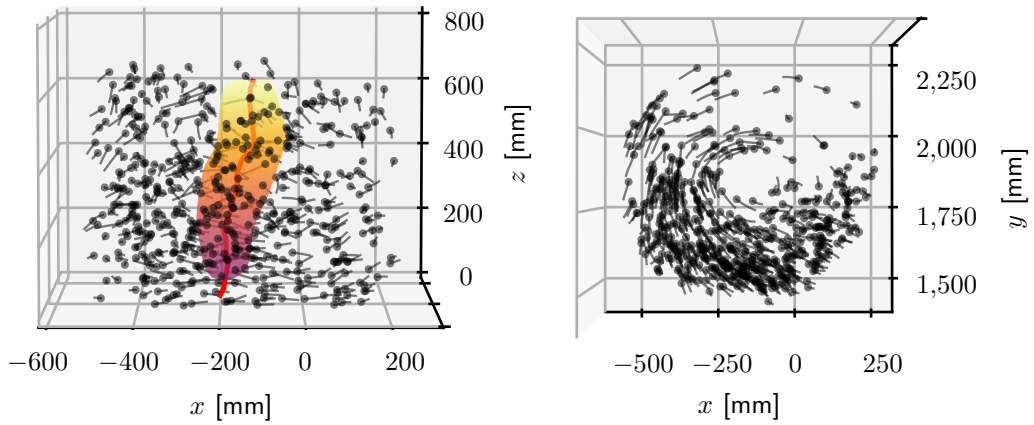

Figure 6: Lagrangian flow field and 50 % isobar of maximum pressure drop of the "primal dust devil-like vortex (PDD)" measured using set-up II. The 50 % isobar of maximum pressure drop defines the diameter of PDD. The red center line connects the points of maximum pressure drop in each horizontal grid plane of the Eulerian field.

to 56 vortices within 2 hours. The following discussion is, thus, solely pointed on the measurements using set-up II.

First of all, the properties of the detected dust devil-like vortices will be described in detail using an explicit example. This vortex, we call it the "primal dust devil-like vortex (PDD)", was also detected by eye. We used this vortex primarily to develop an algorithm to detect this kind of dust devil-like structures. PDD is also examined for its properties and compared to atmospheric dust devils. The structure could be observed over a period of about 14 s until it left the observation area. Hence it was one of the longest observed vortices in this study. Figure 6 shows the Lagrangian velocity field of PDD in top and side view. In order to visualize the diameter of PDD, the 50 % isobar of maximum pressure drop is shown along with the particle tracks. We estimate the diameter with about 200 mm. Unfortunately, we could not determine the actual height of the vortex, since PDD spans the complete height of the observation area and may exceed it.

Figure 7 depicts a horizontal and a vertical cross section through PDD. The horizontal cross section is located 62 mm above the heating plate and shows the streamlines and the pressure field in the vicinity of the vortex. The characteristic pressure drop p as well as the rotational structure is visible quite well. The position of the maximum pressure drop ($\times$) coincides with the position of the maximum vorticity, while the center of rotation of the structure ($+$) is about 50 mm shifted. This shift is typical for atmospheric dust devils which typically migrate along a horizontal path (compare changes of streamlines in Harris and Durran (2006)). In the flow pattern of the vertical cross section (see Fig 7b), the typical side view of a dust devil can be seen. In the lower area ($z < 0.1$ m), air is sucked in from both sides and moves upwards in the central axis of the vortex. A few streamlines lead directly into the bottom ($z = 0$ m), which is, presumably, an artefact of the fine-scale reconstruction algorithm. The pressure drop of about 150 mPa is of the same order of magnitude as in simulations (Giersch & Raasch, 2021), but up to 4 orders of magnitude smaller than for terrestrial dust devils (Metzger, 1999; Tratt et al., 2003).

The pressure and velocity field allow to define the radius of PDD (see Fig. 8). For this purpose, two approaches can be found in literature. First, the radius is defined by the distance between the point of maximum pressure drop p^* (vortex center) and radius,

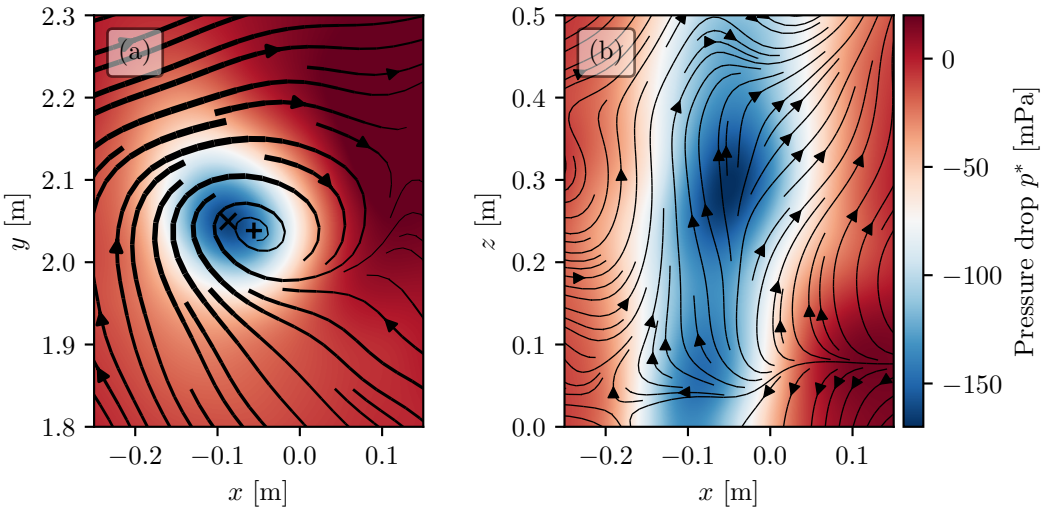

Figure 7: Streamlines and pressure field of PDD in a horizontal (a) and a vertical cross section (b). Both fields are computed using the fine-scale reconstruction algorithm of the commercial software package DaVIS (Jeon et al., 2018). (+) and (×) mark the rotational center and the point of maximum pressure drop, respectively.

where the pressure is just 50 % of this maximum (Lorenz & Jackson, 2016). Second, it can be defined as the distance between the vortex center and the radius where the tangential velocity v_{tan} exhibits a maximum (Balme & Greeley, 2006). In order to simplify the comparison of various dust devil-like structures with different sense of rotation, we always count the tangential velocity as positive in the direction of rotation. We applied both methods to PDD and show the result in Figure 8. One can see that the various radii are quite similar and within the measurement and calculation uncertainties. We also applied this analysis to the tangential velocity v^*_{tan} corrected by subtracting the average migration velocity of the center, but we did not find significant impact on the result.

Next, we will discuss the lateral motion of the dust devil-like vortices which is often referred to as migration. Figure 9 depicts the migration path of the PDD (a), along with the time trace of the pressure drop $p^*(t)$ (b) as well as the migration velocity $v_{migr}(t)$ and the velocity of the background wind v_{av} (c). In order to reduce the scatter of $v_{migr}(t)$ and $p^*(t)$, we smoothed both quantities migration velocity and pressure drop by a sliding average filter of 30 time-steps (1.5 s) and 5 time-steps (0.25 s), respectively. The intensity and direction of the background velocity fairly corresponds to the migration velocity and only shows low variation during the observation period. This is in agreement with atmospheric dust devils which typically move with the background wind (Reiss et al., 2016). During the observation period, the dust devil-like vortex covered a distance of about 2 m and achieved an average migration velocity $\overline{v}_{migr} \approx 147$ mm s^{-1}. Within this period a periodic fluctuation of the pressure drop p^* between −150 mPa and −200 mPa was observed. This is considerably lower than in atmospheric dust devils and is also well below the limit of 30 Pa to lift particles (Lorenz, 2014). The statistical evaluation of data is, analogous to Giersch and Raasch (2021), primarily based on the maximum and minimum values of the individual parameters. Strongly fluctuating values, perhaps induced by measurement or calculation errors, were smoothed with a sliding average filter of 0.25 s before the final values of maxima or minima were identified.

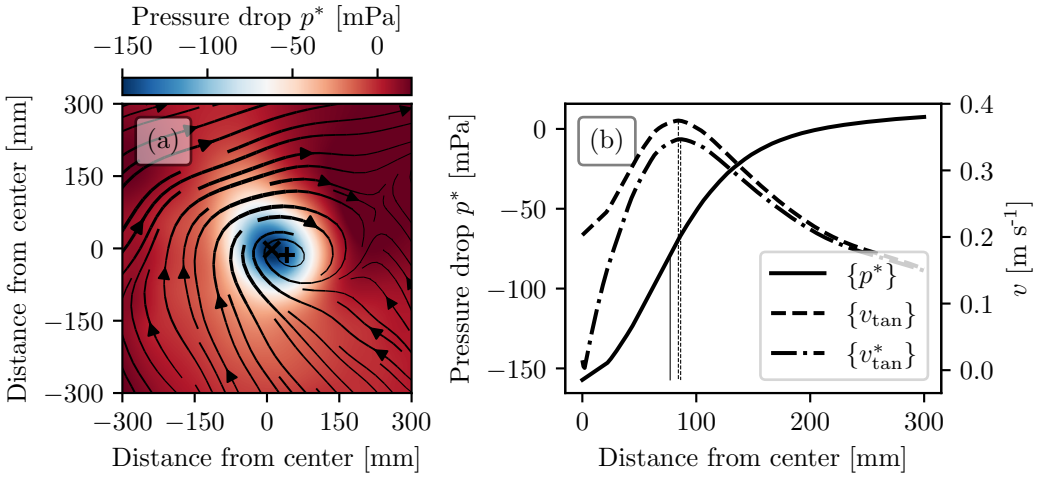

Figure 8: (a) Horizontal cross section through PDD and (b) definitions of radius by tangentially averaged values of pressure drop $\{p^*\}$ as well as natural and corrected average tangential velocity $\{v_{tan}\}$ and $\{v^*_{tan}\}$, respectively.

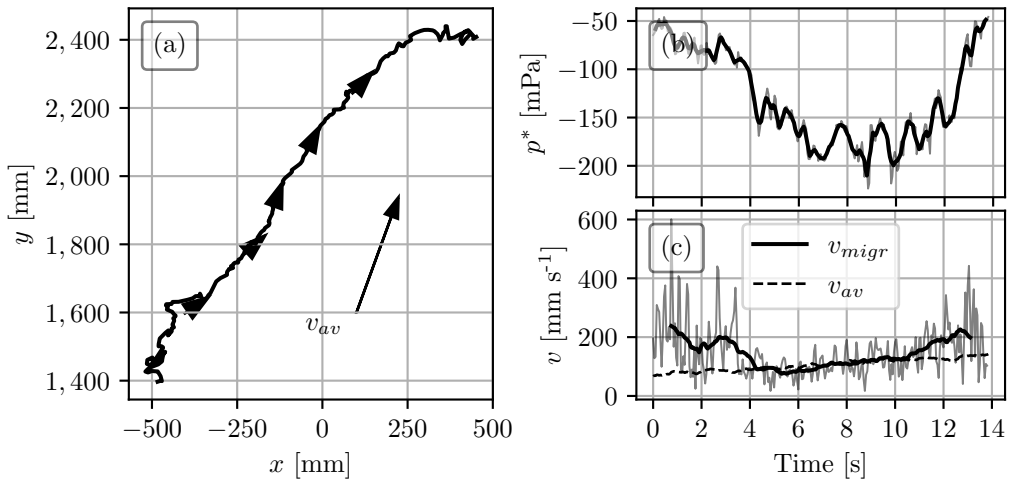

Figure 9: (a) Track of PDD and prevailing background wind direction (v_{av}), (b) pressure drop p^* (raw and transiently smoothed over 5 time-steps) and (c) migration velocity v_{migr} (raw and transiently smoothed over 30 time-steps) as well as the background wind v_{av}.

Having shown horizontal and vertical slides of the instantaneous velocity and pressure field through PDD in Figure 7, Figure 10 depicts the vertical cross section of various parameters averaged over the entire observation period of the structures. Moreover, all structures are re-tilted from their original orientation to one perpendicular to the ground. The pressure drop of PDD (Figure 10a) has its maximum at a height of about 250 mm, and hence, above the tracing point. This is in good agreement with simulations that showed the location of the maximum pressure drop as well located somewhere above the wall (Giersch & Raasch, 2021). It is actually not clear, whether there is a correlation between the distance of the point of maximum pressure drop from the wall and the radius of dust devil-like vortices, but at least, no such correlation is known from atmospheric dust devils (Balme & Greeley, 2006). The dashed lines in Figures 10a indicate the 50 % bound of the maximum pressure drop of the dust devil-like vortex and revealed a mean radius of about 100 mm. The asymmetry in the tangential velocity field (Figure 10c) shows that the dust devil-like vortex was dominantly driven from one side. The buoyancy arises from the ground over the entire observation area and is located centrally above the tracing point. A down flow in the higher center region of the dust devil-like vortex, typical for atmospheric dust devils, could not be observed. But this might be due to the limited field of observation. The radius estimated from the tangential velocity was also about 100 mm. The dashed lines in Figure 10c mark the maximum tangential velocity as boundary of the dust devil-like vortex. The tangential velocity radially increases to a maximum and then decreases again. For the sake of completeness also the vertical vorticity (Figure 10b) as well as the vertical velocity (Figure 10d) are shown. It is to note here, that the streamlines in Figure 10b show the entire flow field, whereas the streamlines in Figure 10d illustrate the flow field after correction by the migration velocity. The streamlines illustrate the flow field in the vertical plane. The flow pattern based on the center of rotation shows the typical flow structure of the lower part of a dust devil. Air is sucked in radially at the bottom and transported upwards. The horizontal velocity was almost zero in the vortex center. Unfortunately, we can not state anything about the upper part of the PDD, since it exceeds the height of the measurement volume in this, higher resolved measurement set-up. This question has to remain open at the moment and has to be answered in future work.

Sinclair (1973) provided an interesting approach to model the tangential velocity of a dust devil and to determine its maximum pressure drop. We also tried to apply this model to the vortices observed in our experiment. Sinclair predicts the tangential velocity by a so-called Rankine vortex which is a solid-body rotation inside a cylinder of radius R_0 and a potential vortex outside the cylinder. The radius R_0 is referred to as the vortex-core radius. Figure 11 shows the radial dependence of tangential velocity of PDD in comparison with the Rankine vortex model. The tangential velocity of the Rankine vortex is determined by equation (7). The estimate of angular velocity ω is defined by the vorticity in the vortex center $\omega = \zeta_z/2$ (Giersch & Raasch, 2021).

$$v_{tan}(r) = \begin{cases} \omega \cdot r & \text{if } r \leq R_0 \\ \frac{\omega R_0^2}{r} & \text{if } r > R_0 \end{cases} \tag{7}$$

The comparison shows a good agreement between the measured tangential velocity (solid line) and the velocity predicted by the Rankine vortex model (dashed line). The overestimation in the range of the vortex radius R_0 is a typical property of this model (Sinclair, 1973). This result is also in good agreement with the simulation of Giersch and Raasch (2021). The pressure drop according to the Rankine vortex p_R^* can be calculated using equation (8) with density of air $\varrho = 1.169$ kg m^{-3} (Giersch & Raasch, 2021; Stephan et al., 2019).

$$p_R^* = \rho \cdot \omega^2 \cdot R_0^2 \tag{8}$$

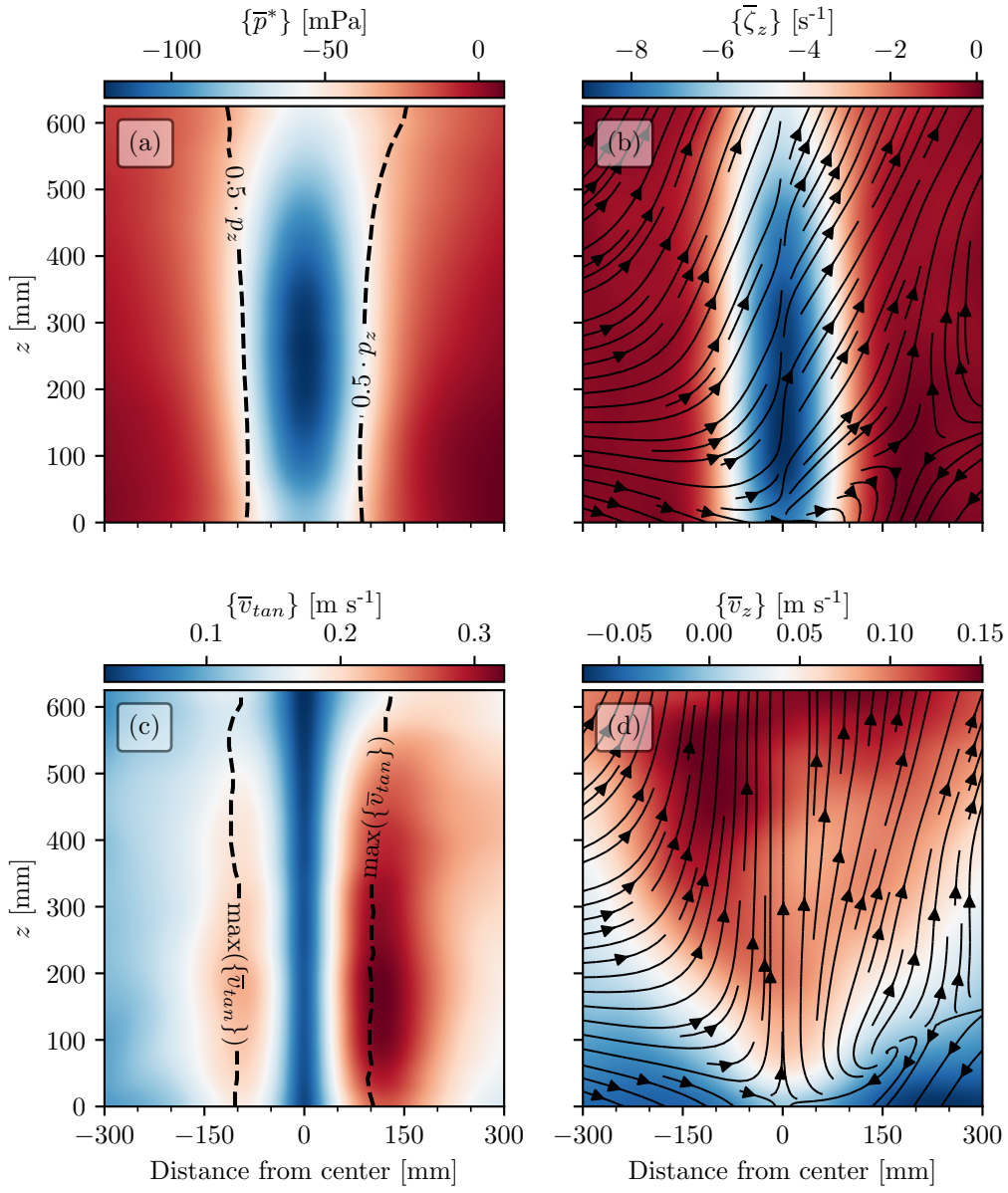

Figure 10: Pressure drop (a), vertical vorticity (b), tangential velocity (c) and vertical velocity (d) of the PDD. All quantities are averaged over the entire observation period. Dashed lines in (a) and (c) mark the diameter of PDD by the 50 % pressure drop and maximum tangential velocity criterion, respectively.

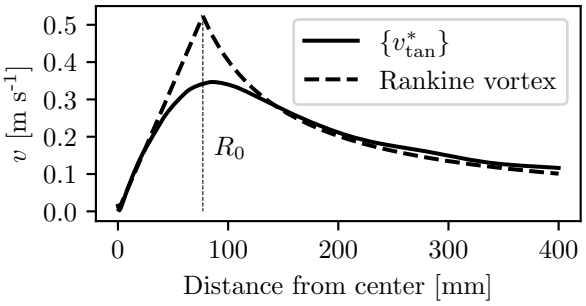

Figure 11: Comparison of the tangential velocity $\{v^*_{tan}\}$ of PDD and a Rankine vortex with $\omega = \zeta_z/2 = 3.35$ s^{-1}.

The so estimated pressure drop of PDD is $p^*_R = 297$ mPa. It is about twice the pressure drop obtained from fine-scale reconstruction of $p^* = 155$ mPa. But, considering the simplicity of the Rankine vortex model and the potential uncertainties of the fine-scale reconstruction, the deviation is not too large.

After definition of all parameters and the comparison of the "primal dust devil-like vortex" PDD with atmospheric dust devils, the following part of the paper will give an overview about the statistics of all dust devil-like vortices observed during our measurements. We start with a collection of all tracks of dust devil-like vortices in the measurement volume which is shown in Figure 12. While Figure 12a summarizes the tracks from the experiment with the overheated area at the center of the heating plate, Figure 12b shows the tracks from the experiment without this. On a first glance, it seems that the hot spot heating enhances the probability of occurrence. But, on closer examination of the experimental conditions, there is no clear correspondence. Comparing simply the number of occurring vortices per time unit, it is indeed lower in the experiment without hot spot heating (18.3 per hour) than in the experiment with it (43.5 per hour). However, the particle density differed from experiment to experiment and we also optimized the particle detection and the tracking algorithm. This leads to an almost doubling of the track rate from typically about 1000 simultaneous tracks in the experiment without hot spot heating to about 1900 in the experiment with hot spot heating. Insofar, the difference might be rather due to the higher detection probability than to a higher rate of occurrence of dust devil-like vortices. It is also seen in the two figures that the majority of the tracks is located in the back third of the observation area and not nearby the hot spot heating, which is another indication that the hot spot may have only an indirect effect on the generation of vortices.

Table 1 summarizes the experimental results. A total of 31 vortices with positive sense of rotation and 21 vortices with negative sense of rotation were detected in both experiments. There is no preferred direction of rotation. This is in agreement with atmospheric dust devils which in general, do not show any preference in the rotation direction. Only very large dust devils might be affected by the Coriolis force and rotate in a preferred direction (Balme & Greeley, 2006). We also compared the specific properties of our experimentally generated dust devil-like vortices with real dust devils. Overall, all properties of experimental vortices were orders of magnitude smaller in comparison to atmospheric dust devils. This was due to the comparably small test volume and the significantly lower Rayleigh number of the experiment, i.e. $Ra \approx 10^{10}$, compared to the Rayleigh number in the convective boundary layer of the atmosphere which is about 10^{18} (Giersch & Raasch, 2021). In a second step of our analysis, we are looking for correlations between various properties, and indeed, such correlations similar to atmospheric dust devils exist. Balme and Greeley

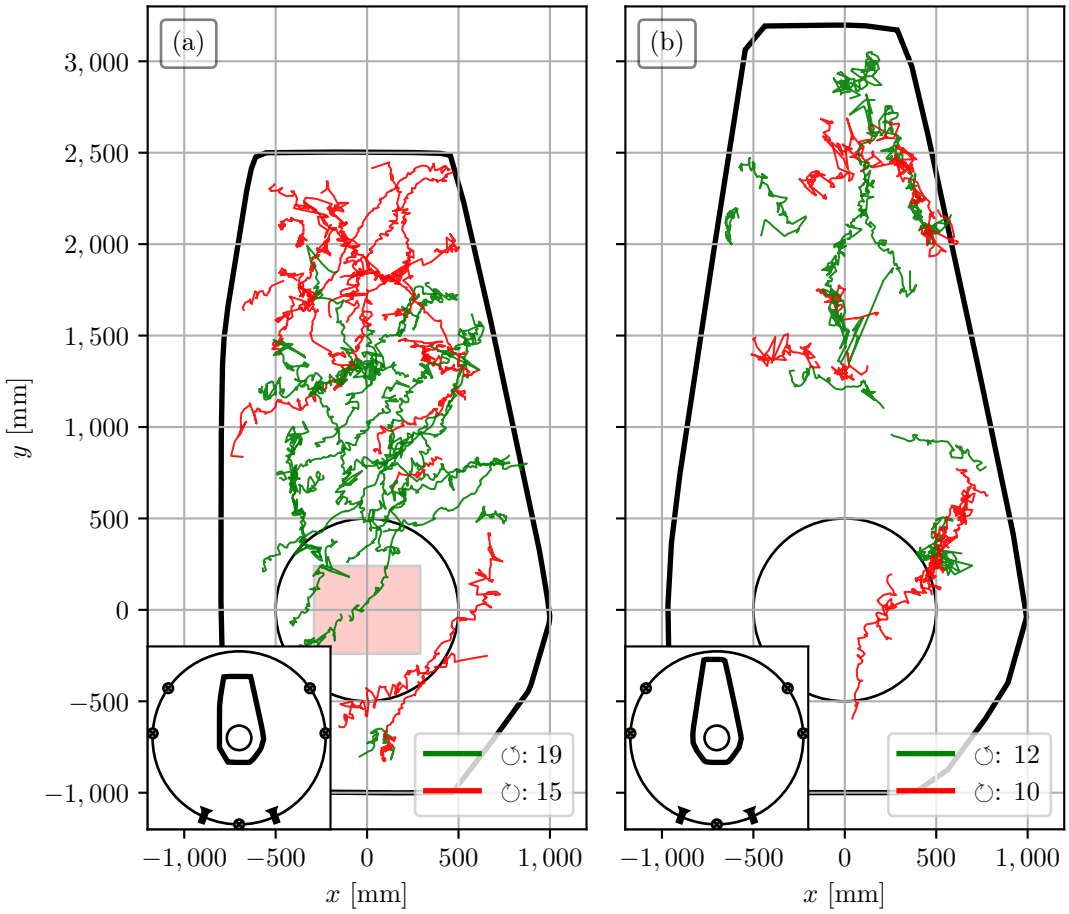

Figure 12: Overview of detected dust devil tracks, (a) with and (b) without hot spot heating. Shown are vortices with positive (green tracks) and negative (red tracks) sense of rotation as well as the observation area (black frame). The red square in a) represents the hot spot heating mat.

Table 1: Summary of dust devil properties. Experiments (exp) I and II were conducted with and without additional hot spot heating, respectively. Statistical values (stats) are given by average (avg), standard deviation (std) and maximum (max).

exp	N	stats	τ	r	$\{\widehat{v}_{migr}\}$	$\{\widehat{v}^*_{tan}\}$	$\{\widehat{v}^*_{rad}\}$	$\{\widehat{v}_z\}$	$\lvert\widehat{p}^*\rvert$	$\left\lvert\widehat{\zeta}_z\right\rvert$
no	-	-	s	mm	cm s^{-1}	cm s^{-1}	cm s^{-1}	cm s^{-1}	mPa	s^{-1}
	34	avg	7.64	132.92	11.67	31.21	8.75	26.36	122.99	13.19
I	↺ 19	std	±3.93	±50.00	±4.00	±5.52	±2.24	±7.83	±41.80	±1.78
	↻ 15	max	14.95	244.97	21.97	40.90	13.79	46.54	214.68	16.30
	22	avg	5.18	129.77	10.66	34.47	9.12	26.16	143.08	13.70
II	↺ 12	std	±2.90	±38.04	±4.09	±5.88	±2.52	±8.47	±43.77	±1.85
	↻ 10	max	12.25	184.22	20.51	44.81	13.89	53.34	221.45	17.03
	56	avg	6.67	131.68	11.28	32.49	8.89	26.28	130.88	13.39
I+II	↺ 31	std	±3.74	±45.33	±4.03	±5.84	±2.34	±8.01	±43.34	±1.81
	↻ 25	max	14.95	244.97	21.97	44.81	13.89	53.34	221.45	17.03

(2006) showed e.g. that atmospheric dust devils exhibit correlations between the maximum buoyancy velocity $\widehat{v}_z$, the radius r and the maximum migration velocity $\widehat{v}_h$. In Figure 13, a correlation matrix of our data is plotted. Each diagram contains a plot of one property against one other and we use these diagrams to determine the strength of the relationship between these two properties. If a regression line can be drawn through the point cloud, the correlation is positive for a rising and negative for a falling line. In further analysis, more sophisticated functions can be used to describe the potential relations between the characteristics, but actually our data set is too small for such an analysis. Anyhow, as closer the pairs of variables are located nearby the regression function as stronger is the correlation. In contrast, homogeneously scattered data points intent no correlation. Correlations are moderate about 0.5 and larger, but strong about 0.9 to 1 (Nachtigall & Wirtz, 2004). A strong correlation between pressure drop p^* and tangential velocity v^*_{tan} could be identified. A power law fit with $f(x) = a \cdot x^b$ revealed an exponent of $b = 1.88$ which is close to the square relationship assumed for the Rankine vortex. Moderate correlations could be identified for pressure drop and radius, vertical vorticity and pressure drop, tangential velocity and radius as well as tangential velocity and vertical vorticity. No or only very weak correlations could be found for the remaining variable pairs. In summary, one can state that at least a qualitative similarity to the relationships of atmospheric dust devil properties could be demonstrated with our experimental work.

Eventually, we wish to discuss the histograms of observation period, radius and pressure drop for a statistical overview. These are shown in Figure 14. Since many of the observed vortices migrate out of the measurement volume, we do not have information on the real lifetime, and thus, we replace it by the observation period τ. The number and position of bins were defined by the Freedman-Diaconis rule (Freedman & Diaconis, 1981). The histogram of observation period also contains a power law fit to the probability density data. This is in agreement with simulations of dust devils which have also shown a lifetime distribution decreasing with a power law. The fit matches the bars in the histogram quite well for lifetimes beyond about 3 s. Interestingly, the frequency of very short-living structures is rather low which is a phenomenon that also appears in the simulations by Giersch et al. (2019). We associate this phenomenon in our experiment with the decreasing detection probability of such very short-living vortices due to the finite density of particles in the observation volume. Furthermore, Sinclair (1969) did not find a clear relationship between frequency of occurrence and lifetime of atmospheric dust devils, the relationship rather

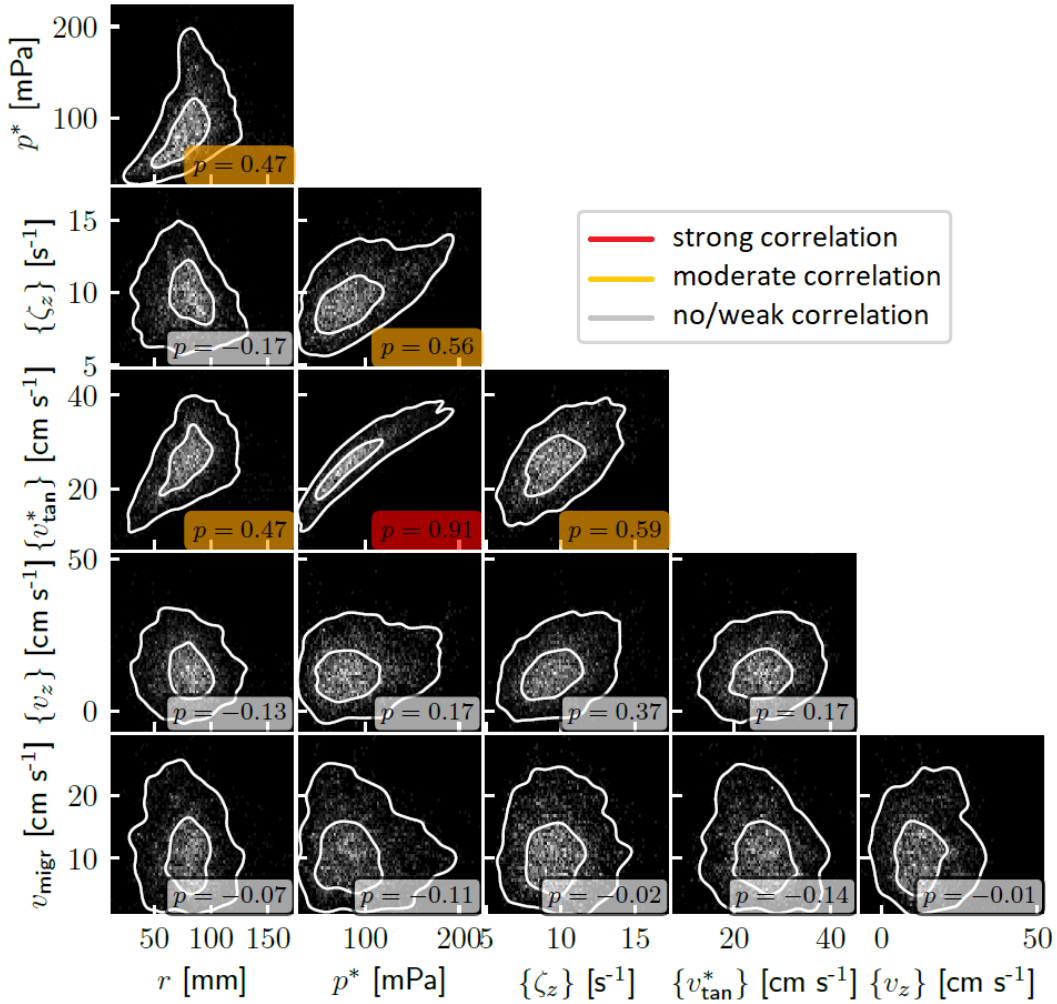

Figure 13: Correlation matrix of all extracted parameters. The inner and outer white line enclose data points within 33 % and 66 % of probability density, respectively.

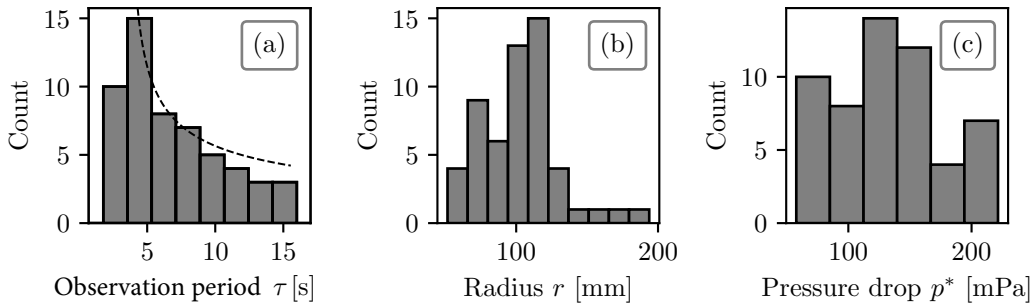

Figure 14: Histograms of observation period (a), radius (b) and pressure drop (c) of all detected dust devil-like vortices and comparison of the observation period distribution to a power law fit.

varies for different diameter regimes. Therefore, the data was fitted by minimizing the L2 norm to the frequency data. The power law fit of the probability density distribution is given by equation (9).

$$p_l(x) = b \cdot (x - c)^a = 0.14 \cdot (x - 3.55)^{-0.47} \tag{9}$$

Further dust devil properties whose probability/frequency of occurrence is assumed to follow a power law are the radius r and the pressure drop p^*. However, we can not confirm this from our study. This is mainly due to the small number of vortices we could analyse in total. Furthermore, the probability of detection rapidly decreases for vortices with a diameter less than ≥ 100 mm. This is clearly seen in Figure 14b, where the frequency goes down for all radii $r < 100$ mm. And last but not least, the fine-scale reconstruction meaning the transformation of the Lagrangian to the Eulerschen flow field may generate some artificial effects that may consequently also have an effect on the determination of the radius and the pressure drop.

Finally, we wish to compare the experimental data with data obtained from direct numerical simulation of turbulent Rayleigh-Bénard convection (Giersch & Raasch, 2021). In the simulation, much more smaller vortices could be detected than in the experiment. This means that the mean property of each is shifted towards these smaller vortices. Table 2 shows the simulation data of the data set *RA1010A3* compared to our experimental data. There are minor variations between experiment and simulations, but in principle, the results are comparable. We used, for instance, a cylindrical convection cell in the experiments with diameter and height of 7.15 m and 2.38 m, respectively, while, simulation was based on a square convection cell with dimension of $4.224 \times 4.224 \times 1.408$ m^3. The Rayleigh numbers of experiment and simulation were quite similar and amounted to $Ra \approx 10^{10}$. Considerably more structures could be detected in the simulation, however, on a much shorter time-scale. The relationship between pressure drop and observation period as well as pressure drop and vorticity were similar in both experiment and simulation, while the size of dust devils and frequency of occurrence are anti-correlated. Unlike in the simulation we observed moderate correlations between vortex radius and observation period as well as pressure drop, respectively. In summary, one can state that simulations may visualize very small structures much better than in experiments. Experiments are clearly beneficial to study the very rarely occurring larger dust devil-like structures, since the simulation period (100 s) is simply too short for this. Taken into account the slightly different data

Table 2: Comparison of simulation (sim) and experiment (exp). Statistical values (stats) are given by average (avg), standard deviation (std) and maximum (max).

	N	stats	τ	r	$\{\widehat{v}_{\mathrm{migr}}\}$	$\{\widehat{v}^*_{tan}\}$	$\{\widehat{v}^*_{rad}\}$	$\{\widehat{v}_z\}$	$\lvert\widehat{p}^*\rvert$	$\left\lvert\widehat{\zeta}_z\right\rvert$
	-	-	s	mm	cm s^{-1}	cm s^{-1}	cm s^{-1}	cm s^{-1}	mPa	s^{-1}
	865	avg	0.82	6.47	15.3	32.8	18.1	13.5	255	310
sim	↺ 434	std	±1.21	±3.13	±6.74	±13.3	±7.76	±3.19	±235	±125
	↻ 431	max	18.8	26.3	44.3	101	52.6	32.2	1708	928
	56	avg	6.67	131.68	11.28	32.49	8.89	26.28	130.88	13.39
exp	↺ 31	std	±3.74	±45.33	±4.03	±5.84	±2.34	±8.01	±43.34	±1.81
	↻ 25	max	14.95	244.97	21.97	44.81	13.89	53.34	221.45	17.03

base, the agreement between the data is fairly well and deviations can be reduced in future work by improving both, the experimental basis and the numerical set-up.

4 Summary and outlook

We could experimentally demonstrate that dust devil-like vortices spontaneously arise in turbulent Rayleigh-Bénard convection. To our knowledge, it was the first time experimental survey to simulate the genesis of dust devil-like vortices in a laboratory experiment which mimics the convective atmospheric boundary layer quite closely and gets by without any artificial input of rotation. In our large-scale experiment, dust devil-like vortices are measured and identified using the particle tracking velocimetry technique. Furthermore, our experimental set-up permits measuring periods of several hours and enables us to detect flow structures which rarely appear. Within an observation period of two hours (this is the period whose analysis is already finished) we could detect 56 dust devil-like vortices in total. Their properties coincide quite well with those structures identified in very recent direct numerical simulations by Giersch and Raasch (2021) as well as they show similarity to atmospheric dust devils. The size of our experimentally generated dust devil-like vortices starts at about one decimeter and ranges up to about one meter. This is fairly greater dimension than in numerical simulations, but still smaller as in the atmosphere. One limitation of our actual experiment is the maximum number of tracers / soap bubbles per volume unit at the same time which is of the order of 1 dm^{-3}. In future experiments, this should be increased by at least one order of magnitude to enable highly reliable measurement in full space of the "Barrel of Ilmenau" capturing also the larger dust devil-like vortices and reduce uncertainty in transformation of the Langrangian to the Eulerian velocity field. This will improve and expand the statistical analysis to a broader range of structure size.

Acknowledgments

The authors are grateful to the German Research Foundation (Deutsche Forschungsgemeinschaft – DFG) for financial support, grant no. 387703749. Sabine Scherge is acknowledged for technical assistance to run the experiments. Furthermore, we thank Alice Loesch for setting up the experimental testing method and gathering preliminary results.

References

Balme, M., & Greeley, R. (2006). Dust devils on Earth and Mars. *Reviews of Geophysics*, *44*(3). doi: https://doi.org/10.1029/2005RG000188

Balme, M., Greeley, R., Mickelson, B., Iversen, J., Beardmore, G., & Metzger, S. (2001). A Laboratory Scale Vortex Generator for Simulation of Martian Dust Devils. In *AGU Fall Meeting Abstracts* (Vol. 2001, pp. P31A–0542).

Barcilon, A. (1967). A theoretical and experimental model for a dust devil. *Journal of Atmospheric Sciences*, *24*(5), 453–466.

Bell, F. (1967). *Dust devils and aviation, Meteorol* (Tech. Rep.). Note 27, Commonwealth of Australia, Bureau of Meteorology.

Brooks, H. B. (1960). SHORTER CONTRIBUTIONS: ROTATION OF DUST DEVILS. *Journal of the Atmospheric Sciences*, *17*(1), 84–86.

Carroll, J. J., & Ryan, J. A. (1970). Atmospheric vorticity and dust devil rotation. *Journal of Geophysical Research (1896-1977)*, *75*(27), 5179-5184. doi: https://doi.org/10.1029/JC075i027p05179

Chan, P. W., & Li, Q. (2021). Observation and numerical simulation of a dust devil at the Hong Kong International Airport. *Meteorologische Zeitschrift*, *30*(6), 533–543.

Cortese, T., & Balachandar, S. (1993). Vortical nature of thermal plumes in turbulent convection. *Physics of Fluids A: Fluid Dynamics*, *5*(12), 3226–3232.

Du Puits, R., Resagk, C., & Thess, A. (2013). Thermal boundary layers in turbulent Rayleigh–Bénard convection at aspect ratios between 1 and 9. *New Journal of Physics*, *15*(1), 013040.

Fiedler, B. H., & Kanak, K. M. (2001). Rayleigh-Bénard convection as a tool for studying dust devils. *Atmospheric Science Letters*, *2*(1-4), 104–113.

Fitzjarrald, D. (1973). A laboratory simulation of convective vortices. *Journal of Atmospheric Sciences*, *30*(5), 894–902.

Flower, W. D. (1936). *Sand devils*. HM Stationery Office.

Fodor, K., Mellado, J. P., & Wilczek, M. (2019). On the role of large-scale updrafts and downdrafts in deviations from Monin–Obukhov similarity theory in free convection. *Boundary-layer meteorology*, *172*(3), 371–396.

Freedman, D., & Diaconis, P. (1981). On the histogram as a density estimator: L 2 theory. *Zeitschrift für Wahrscheinlichkeitstheorie und verwandte Gebiete*, *57*(4), 453–476.

Giersch, S., Brast, M., Hoffmann, F., & Raasch, S. (2019). Toward large-eddy simulations of dust devils of observed intensity: Effects of grid spacing, background wind, and surface heterogeneities. *Journal of Geophysical Research: Atmospheres*, *124*(14), 7697–7718.

Giersch, S., & Raasch, S. (2021). Evolution and Features of Dust Devil-Like Vortices in Turbulent Rayleigh-Bénard Convection—A Numerical Study Using Direct Numerical Simulation. *Journal of Geophysical Research: Atmospheres*, *126*(7), e2020JD034334.

Greeley, R., Balme, M. R., Iversen, J. D., Metzger, S., Mickelson, R., Phoreman, J., & White, B. (2003). Martian dust devils: Laboratory simulations of particle threshold. *Journal of Geophysical Research: Planets*, *108*(E5).

Harris, L., & Durran, D. (2006). Streamlines vs. Trajectories in a Translating Rankine Vortex. *https://atmos.uw.edu/ durrand/animations/vort505/vortanim1.html.*.

Hess, G. D., & Spillane, K. T. (1990). Characteristics of dust devils in Australia. *Journal of Applied Meteorology and Climatology*, *29*(6), 498–507.

Idso, S. B., & Kimball, B. A. (1974). Tornado or dust devil: The enigma of desert whirlwinds. *American Scientist*, *62*(5), 530–541.

Ives, R. L. (1947). Behavior of dust devils. *Bulletin of the American Meteorological Society*, *28*(4), 168–174.

Jackson, B., Lorenz, R., Davis, K., & Lipple, B. (2018). Using an Instrumented Drone to Probe Dust Devils on Oregon's Alvord Desert. *Remote Sensing*, *10*(1), 65.

Jeon, Y., Schneiders, J., Müller, M., Michaelis, D., & Wieneke, B. (2018). 4D flow

field reconstruction from particle tracks by VIC+ with additional constraints and multigrid approximation. In *Proceedings 18th International Symposium on Flow Visualization.*

Kanak, K. M. (2005). Numerical simulation of dust devil-scale vortices. *Quarterly Journal of the Royal Meteorological Society: A journal of the atmospheric sciences, applied meteorology and physical oceanography*, *131*(607), 1271–1292.

Lienhard, I., & John, H. (2005). *A heat transfer textbook*. phlogiston press.

Loesch, A., & du Puits, R. (2020). Experimental investigation of Dust Devil like vortices with 3D particle tracking velocimetry. In *EGU General Assembly Conference Abstracts* (p. 22451).

Loesch, A., & du Puits, R. (2021). The Barrel of Ilmenau: A large-scale convection experiment to study dust devil-like flow structures. *Meteorologische Zeitschrift*, 89–97.

Lorenz, R. D. (2014). Vortex encounter rates with fixed barometer stations: Comparison with visual dust devil counts and large-eddy simulations. *Journal of the Atmospheric Sciences*, *71*(12), 4461–4472.

Lorenz, R. D., & Jackson, B. K. (2016). Dust devil populations and statistics. *Space Science Reviews*, *203*(1), 277–297.

Lorenz, R. D., Neakrase, L. D., & Anderson, J. D. (2015). In-situ measurement of dust devil activity at La Jornada Experimental Range, New Mexico, USA. *Aeolian Research*, *19*, 183–194.

Ludlum, D. M. W. and Society, N. A. (1991). *National Audubon Society Field Guide to North American Weather*. A. A. Knopf.

Mattsson, J. O., Nihlén, T., & Yue, W. (1993). Observations of dust devils in a semi-arid district of southern Tunisia. *Weather*, *48*(11), 359–363.

Maxworthy, T. (1972). On the structure of concentrated, columnar vortices. *Astronaut. Acta*, *17*, 363–374.

McGinnigle, J. B. (1966). DUST WHIRLS IN NORTH-WEST LIBYA. *Weather*, *21*(8), 272–276.

Metzger, S. M. (1999). *Dust devils as aeolian transport mechanisms in southern Nevada and the Mars Pathfinder landing site* (Unpublished doctoral dissertation). UNIVERSITY OF NEVADA, RENO.

Morton, B. R. (1966). Geophysical vortices. *Progress in Aerospace Sciences*, *7*, 145–194.

Mullen, J. B., & Maxworthy, T. (1977). A laboratory model of dust devil vortices. *Dynamics of Atmospheres and Oceans*, *1*(3), 181–214.

Nachtigall, C., & Wirtz, M. A. (2004). *Wahrscheinlichkeitsrechnung und Inferenzstatistik*. Juventa-Verlag Weinheim.

Neakrase, L. D., & Greeley, R. (2010). Dust devil sediment flux on Earth and Mars: Laboratory simulations. *Icarus*, *206*(1), 306–318.

Ohno, H., & Takemi, T. (2010). Mechanisms for intensification and maintenance of numerically simulated dust devils. *Atmospheric Science Letters*, *11*(1), 27–32.

Pandey, A., Scheel, J. D., & Schumacher, J. (2018). Turbulent superstructures in Rayleigh-Bénard convection. *Nature communications*, *9*(1), 1–11.

Raasch, S., & Franke, T. (2011). Structure and formation of dust devil–like vortices in the atmospheric boundary layer: A high-resolution numerical study. *Journal of Geophysical Research: Atmospheres*, *116*(D16).

Reiss, D., Fenton, L., Neakrase, L., Zimmerman, M., Statella, T., Whelley, P., ... Balme, M. (2016). Dust devil tracks. *Space Science Reviews*, *203*(1), 143–181.

Renno, N. O., Abreu, V. J., Koch, J., Smith, P. H., Hartogensis, O. K., De Bruin, H. A. R., ... Carswell, A. (n.d.). MATADOR 2002: A pilot field experiment on convective plumes and dust devils, journal = Journal of Geophysical Research: Planets, volume = 109, number = E7, pages = , keywords = aerosol, convection, dust devil, doi = https://doi.org/10.1029/2003JE002219, year = 2004.

Ringrose, T. (2005). Inside dust devils. *Astronomy & Geophysics*, *46*(5), 5–16.

Schanz, D., Gesemann, S., & Schröder, A. (2016). Shake-The-Box: Lagrangian particle tracking at high particle image densities. *Experiments in fluids*, *57*(5), 1–27.

Sinclair, P. C. (1965). On the rotation of dust devils. *Bulletin of the American Meteorological Society*, *46*(7), 388–391.

Sinclair, P. C. (1969). General Characteristics of Dust Devils. *Journal of Applied Meteorology*, *8*(1), 32-45. doi: 10.1175/1520-0450(1969)008

Sinclair, P. C. (1973). The Lower Structure of Dust Devils. *Journal of Atmospheric Sciences*, *30*(8), 1599 - 1619. doi: 10.1175/1520-0469(1973)030⟨1599:TLSODD⟩2.0.CO;2

Sorbjan, Z. (1996). Joint effects of subgrid-scale diffusion and truncation errors in large-eddy simulations of the convective boundary layer. *Boundary-layer meteorology*, *79*(1), 181–189.

Spiga, A., Barth, E., Gu, Z., Hoffmann, F., Ito, J., Jemmett-Smith, B., ... others (2016). Large-eddy simulations of dust devils and convective vortices. *Space Science Reviews*, *203*(1), 245–275.

Stephan, P., Kabelac, S., Kind, M., Mewes, D., Schaber, K., & Wetzel, T. (2019). *VDI-Wärmeatlas: Fachlicher Träger VDI-Gesellschaft Verfahrenstechnik und Chemieingenieurwesen*. Springer-Verlag.

Sullivan, P. P., McWilliams, J. C., & Moeng, C.-H. (1994). A subgrid-scale model for large-eddy simulation of planetary boundary-layer flows. *Boundary-Layer Meteorology*, *71*(3), 247–276.

Tratt, D. M., Hecht, M. H., Catling, D. C., Samulon, E. C., & Smith, P. H. (2003). In situ measurement of dust devil dynamics: Toward a strategy for Mars. *Journal of Geophysical Research: Planets*, *108*(E11).

Wieneke, B. (2018). Improvements for volume self-calibration. *Measurement Science and Technology*, *29*(8), 084002.

Williams, N. R. (1948). Development of dust whirls and similar small-scale vortices. *Bulletin of the American Meteorological Society*, *29*(3), 106–117.